https://doi.org/10.1007/s41230-025-4283-y

Structural die casting application of a heat treated free aluminum-silicon alloy

Xiang-yi Jiao[1, 2], Peng-yue Wang[3], Yi-xian Liu[4], Wen-ning Liu[4], and *Shou-mei Xiong[4]

1. School of Materials Science and Engineering, Northeastern University, Shenyang 110819, China

2. Key Laboratory of Lightweight Structural Materials, Liaoning Province, Northeastern University, Shenyang 110819, China

3. China FAW Foundry Co., Ltd., Changchun 130013, China

4. School of Materials Science and Engineering, Tsinghua University, Beijing 100084, China

Abstract: The advancement of integrated die-casting technology calls for high-strength, high-ductility heat-treatment-free Al alloys. This study investigates the use of a new AlSiFeMnVTiSrZr heat-treatment-free die-casting alloy for shock tower manufacturing. Results show the alloy has excellent overall mechanical properties, but significant regional differences in microstructure and performance are found in the shock tower casting: Far-gate Position 6 has almost no externally solidified crystals (ESCs), whereas dense coarse dendritic ESCs exist in the center of near-gate Position 5. The fracture surface of Position 6 shows a steeper slope, while Position 5 has a rough crack propagation platform. Far-gate Position 6 also has higher porosity (nearly triple that of near-gate Region 5) and larger average pore size. Analysis reveals microstructural heterogeneity between near- and far-gate regions strongly influences mechanical performance. Notably, coarse dendritic ESCs in the near-gate region restrict grain boundary strengthening, leading to lower yield strength despite low porosity. Conversely, while fine grains in the far-gate region could enhance grain boundary strengthening, abundant porosity acts as crack initiation sites, severely reducing ductility. These findings provide theoretical guidance for evaluating integrated die-cast component performance.

Keywords: AlSiFeMnVTiSrZr; high-pressure die-casting; shock tower; heat-treatment free

CLC numbers: TG146.21 **Document code:** A **Article ID:** 1672-6421(2026)02-197-08

1 Introduction

Lightweight design has emerged as a global trend in automotive development, driven by energy-saving and environmental-protection imperatives[1]. Automakers achieve the challenging goals of reducing fuel consumption and carbon emissions by manufacturing lightweight vehicle bodies[2]. In recent years, aluminum alloy has gained prominence in automotive body applications. It features high specific strength and cost-effectiveness, making it one of the top choices for automotive lightweight[3, 4]. Aluminum alloy parts are commonly used in vehicle body include chassis, anti-collision beam, engine block, heat exchanger, and shock tower, among others[1, 4, 5]. As lightweight design becomes increasingly important in vehicle body development, the application of aluminum alloys continues to grow annually, establishing their significant role in the automotive industry[6]. Common aluminum alloy series include Al-Si[7], Al-Mg[8], Al-Cu[9], and Al-Zn systems[10]. Due to the addition of Si, Al-Si system alloys exhibit excellent casting properties and strong bearing capacity, especially for near-eutectic Al-Si casting alloys[11]. For example, Silafont-36 (AlSi10MnMg alloy) exhibits a high cost-performance ratio and is widely used in its heat-treated condition[12]. However, the heat treatment process is associated with high energy consumption, which contradicts the principles of efficient energy utilization and environmental protection. Achieving high toughness in the heat treatment-free state is of great significance for the development of new Al-Si alloys. This advancement undoubtedly imposes higher demands on the design and optimization of Al-Si alloy materials.

Heat-treatment free Al-Si alloys usually exhibit a lower strength and poor plasticity. Many methods have been tried

*Shou-mei Xiong

Male, Ph. D., Professor. Research interests: Al and Mg alloy high pressure die casting and microstructure simulation during solidification.

E-mail: smxiong@tsinghua.edu.cn

Received: 2024-12-18; Revised: 2025-05-13; Accepted: 2025-07-14

to improve their strength and plasticity in recent years. Fine grain strengthening can achieve synergistic improvement of strength and plasticity. Basavakumar et al.[13] found finer Al dendrites obtained by adding 1% Al-1Ti-3B promoted the strength from 163 MPa to 184 MPa and elongation from 6.5% to 10%. The effective modification of eutectic Si particles is also an important way to improve the properties. Tempel et al.[14] found adding Sr would induce twinning and promote the formation of fibrous Si particles. In addition, Zamani et al.[15] found the minor addition of Zr, Ni, Ti, V, Cr, La, Y, and Nb elements significantly increased the dispersed second phases, thus improving the service life of the alloy. Trace multi-component alloying becomes a potential for improving the properties of heat-treatment free Al-Si alloys.

High pressure die casting (HPDC) is one of the most effective casting processes for producing parts with high dimensional accuracy, small surface roughness, and complex shapes[16]. It has good forming capability, high production efficiency, and good economic index. Three key stages in HPDC include low-speed injection stage, high-speed filling stage, and intensification pressure stage. During low-speed injection, the melt moves slowly in the shot sleeve, causing externally solidified crystals (ESCs) to precipitate on the sleeve wall and grow into large dendrites. In the high-speed filling stage, the fast-moving liquid carries ESCs into the die cavity, where they are broken and remelted due to the strong impact of the filling flow. After finishing the cavity filling, a high intensification pressure is applied by plunger for obtaining the high density die castings. Affected by the above process features, large-scale porosity and coarse primary phases are easily to form in die-casting parts, accelerating casting failure during service. Zhang et al.[17] found pores originated from air entrainment were inevitable and it significantly reduced casting mechanical properties. Zheng et al.[18] found the initiation and propagation of cracks were all related to coarse primary ESCs. In addition, the actual mold structure of large vehicle die-casting parts is complex, and the microstructure and mechanical properties of large-sized castings vary at different sampling positions, which requires a profound study.

In this study, a newly developed heat-treatment free die-casting AlSiFeMnVTiSrZr alloy was proposed and its application on shock tower was investigated. Furthermore, the microstructure and mechanical properties of near-gate and far-gate plates at complex locations of the shock tower were compared.

2 Experimental procedures

2.1 Materials and process parameters

A newly developed heat-treatment free hypoeutectic Al-Si alloy, AlSiFeMnVTiSrZr, was utilized in this experiment and its chemical compositions are listed in Table 1. Figure 1(a) shows the three-dimensional structure of the shock tower, in which the thickness of the biscuit was 30 mm and the diameter was 120 mm. Six sampling positions were selected for mechanical property test, of which Positions 1 and 6 are far away from the gate, while Positions 3, 4, and 5 are near the gate, as shown in Figs. 1(b) and (c). The thicknesses of the plates sampled at Positions 1 to 6 are 3.00 mm, 2.99 mm, 2.11 mm, 2.63 mm, 3.04 mm, and 2.53 mm, respectively. The HPDC experiment was carried out on a 2800 t Frech high vacuum die-casting machine. The key process parameters, including slow-shot speed, fast-shot speed, vacuum condition, and pouring temperature, adopted in the experiment are shown in Table 2. During the die-casting process, the punch underwent a uniformly accelerated motion. It transitioned from slow-shot speed stage 1 to slow-shot speed stage 2 and then to slow-shot speed stage 3, generating multi-stage slow-shot speeds within

Table 1: Chemical composition of AlSiFeMnVTiSrZr alloy (wt.%)

Elements	Si	Fe	Mn	V	Ti	Sr	Zr	Al
Nominal	8.5–9.5	< 0.15	0.4–0.6	0.15–0.25	0.05–0.15	0.02–0.04	0.15–0.25	Bal.
Actual	8.95	0.12	0.48	0.15	0.08	0.02	0.15	Bal.

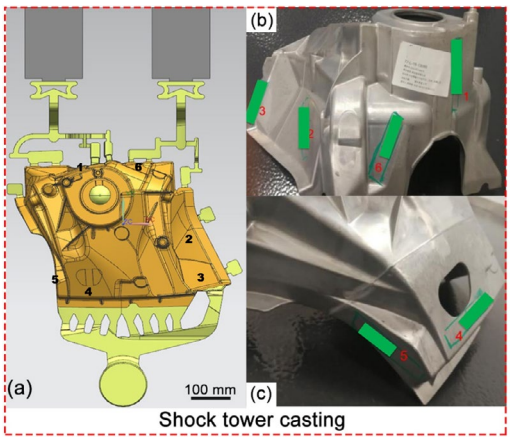

Fig. 1: Configuration of HPDC shock tower casting (a) and plates extraction locations for tensile test (b)–(c)

Table 2: Key processing parameters in HPDC experiments

Pouring temperature (°C)	Slow-shot speed ($m \cdot s^{-1}$)	Fast-shot speed ($m \cdot s^{-1}$)	Vacuum condition
710	0, 0.2, 0.44	5.5	On

the shot sleeve. At the same time, the pouring temperature for shock tower experiment was increased to 710 °C for preventing the melt from early solidification in the process of filling the thin wall of complex structure. For observing the microstructure and defects in HPDC alloys, optical microscopy (OM), scanning electron microscopy (SEM), and synchrotron radiation imaging technology were used.

2.2 Microstructure observation and tensile test

For metallography observation of the cross section, water sandpapers of #200–#2000 were used in order. Following mechanical mounting, polishing, and ultrasonic cleaning, the plates surface was etched using Murakami reagent (10 g NaOH, 5 g $K_3[Fe(CN)_6]$ and 60 mL H_2O) for 30 s. For the fractured plates, synchrotron radiation imaging was employed to examine both the fracture morphology and the subsurface porosity.

The synchrotron radiation imaging was performed at an operating voltage of 100 kV and a current of 110 μA. Given the dimensions of the fractured plates, a voxel size of 3 μm was selected, and 1,100 projections were acquired over a 360° rotational scan. The projections were then processed using Vgstudio Max software for phase retrieval, contrast enhancement, and noise reduction, yielding 2,400 16-bit tomographic slices. These slices were subsequently imported into Avizo® for three-dimensional visualization and analysis. In addition, Avizo® software and manual screening of metallographic images were used to accurately identify ESCs (their size was setting over 10 μm). Tensile tests were conducted on a WDW 3020 electronic universal testing machine with a 25 mm extensometer. The tensile rate was set at 1 $mm \cdot min^{-1}$. To ensure accuracy, tensile plates were taken from three shock towers fabricated with identical process parameters.

3 Results and discussion

3.1 Mechanical properties of HPDC AlSiFeMnVTiSrZr alloy

Figure 2 and Table 3 show the mechanical properties of as-cast AlSiFeMnVTiSrZr extracted from shock tower. Our targets for heat-treatment-free alloy development are: yield strength exceeds 120 MPa, ultimate tensile strength higher than 260 MPa, and elongation higher than 10%. For the as-cast AlSiFeMnVTiSrZr alloy, the strength and elongation meet the target values, except for the yield strength at Positions 1 and 5, and the elongation at Position 6. Comparatively, the yield

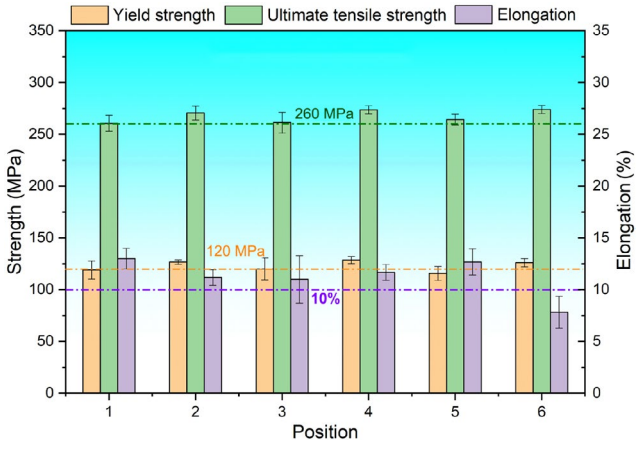

Fig. 2: Mechanical properties of as-cast AlSiFeMnVTiSrZr extracted from shock tower

Table 3: Mechanical properties of as-cast AlSiFeMnVTiSrZr

Position	YS (MPa)	UTS (MPa)	EL (%)
1	119.0±8.7	260.7±7.8	13.0±1.0
2	126.7±2.1	270.7±6.7	11.2±0.8
3	120.0±10.6	261.3±10.1	11.0±2.3
4	128.7±3.5	273.7±4.2	11.7±0.8
5	115.7±6.7	264.3±5.0	12.7±1.3
6	126.0±4.0	274.0±4.0	7.8±1.5

strength at Position 1 is 119 MPa, nearly hitting the 120 MPa target. The yield strength at Position 5 misses the mark by 4.3 MPa. At Position 6, the elongation is 7.8%, 2.2% lower than the set value, indicating a relatively low result. For explaining the reasons for above results, the microstructures at Positions 5 and 6 were extracted and analyzed.

3.2 Microstructure difference in typical sampling positions of shock tower

Figures 3(a) and (b) show the optical micrographs of Positions 5 and 6 in shock tower, respectively. Position 5 near the gate exhibits a skin layer of approximately 130 μm thick, and a high area fraction of fine Al grains is distributed in this area [Fig. 3(c)]. After calculation, as shown in Figs. 3(g–i), the average diameter and area fraction of Al grains in the skin layer is 5 μm and 43.8%, respectively. Near the skin layer, the obvious microstructure difference is observed and the size and spacing of Al grains rapidly increase. The microstructure in Position 6 exhibits nearly no ESCs [Fig. 3(b)] and from surface to center, fine Al grains maintain a high area fraction, as shown in Figs. 3(d) and (f), but the Al grains in surface exhibit a wider spacing resulted by the high-speed liquid impact. In addition, obvious micropores can be identified in Fig. 3(b). In comparison, in Fig. 3(e), the coarse irregular ESCs densely distribute in the central area. They connect with each other, forming a large ESC network [Fig. 3(a)]. In die casting process, the relatively lower cooling rate in the shot sleeve promotes the dendrite growth of ESCs. When the fast shot speed is triggered, high-speed liquid rapidly fills the die cavity carrying ESCs, which are broken, remelt and finally preserved in die castings. Near the die cavity surface, the ESCs experience intense liquid flow impact and fragment into globular shapes. In contrast, in the central zone where the solid fraction is lower during solidification, the ESCs are surrounded by a relatively quiescent melt, allowing their original morphology to be largely preserved.

Figures 4(a) and (b) show the scanning electron micrograph of surface microstructure in Positions 6 and 5, respectively. In Fig. 4(a), fine Al grains, eutectic Si particles, and precipitates are present and a pore close to 20 μm is marked and enlarged as shown in Fig. 4(e). In Fig. 4(b), an obvious interface is observed between the chilling skin layer and normal solidified zone. The difference between the two zones is the grain size.

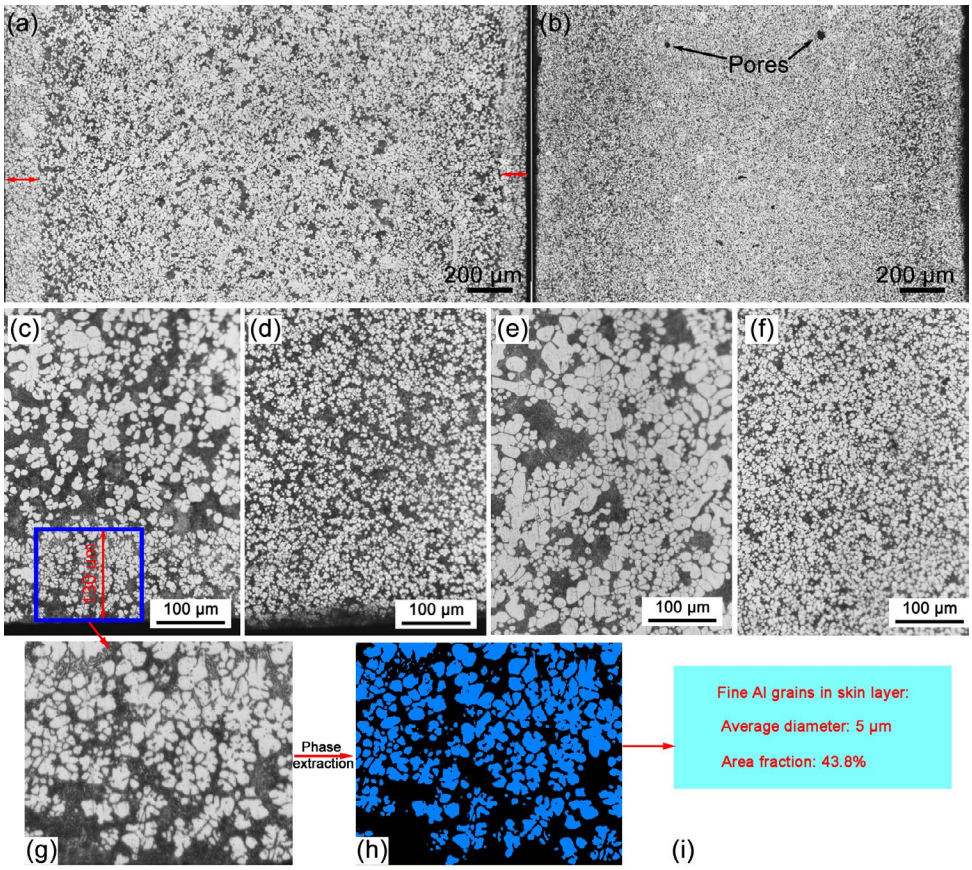

Fig. 3: Optical micrographs of Position 5 (a) and Position 6 (b), their corresponding surface areas (c, d) and central areas (e, f), respectively. Enlarged view of the skin layer (g) and its phase extraction (h), and average diameter and area fraction of fine Al grains (i)

Larger-sized primary α-Al and higher segregation appear in the normal solidified zone.

Approaching to the center, Al grains still exhibit small size, and multiple precipitate including iron-rich phase, and plate shape $(AlSi)_3ZrTi$ emerges in the boundary of Al grains in Fig. 4(c). As shown in Fig. 4(f), multiple $(AlSi)_3ZrTi$ precipitates with a plate shape are densely distributed and interlocked each other, while their size exhibits significant differences. In Fig. 4(d), the main phases comprise of large-sized ESCs and fiber Si particles. In addition, fewer iron-rich phases and $(AlSi)_3ZrTi$ are distributed along ESC boundary, but their size is larger especially the iron-rich phases, as shown in Fig. 4(g).

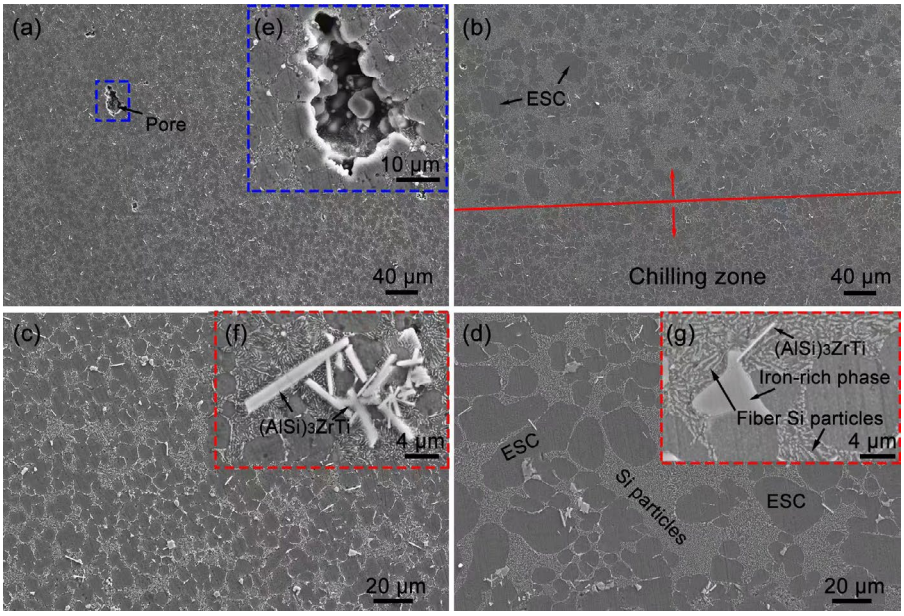

Fig. 4: Scanning electron micrographs of surface microstructure: (a, e) Position 6; (b) Position 5; central microstructure: (c, f) Position 6; (d) Position 5; and (g) $(AlSi)_3ZrTi$ and iron-rich phase precipitates

3.3 Difference of fracture characteristics

Figures 5(a) and (b) show the whole casting fracture morphology of Positions 6 and 5, respectively. In Fig. 5(a), a flat fracture is present and large-scale irregular shrinkages and relatively regular gas pore are distributed in local fracture, as shown in Figs. 5(a1) and (a2). No obvious crack source can be identified. In Fig. 5(b), a rough fracture morphology covers nearly the whole central fracture and this area inside the red wireframe contains some shrinkages, as shown in Fig. 5(b1). The formation of rough fracture is closely associated with the transgranular fracture mode of enriched soft ESCs. Further enlarging the fracture, brittle iron-rich phase and fine dimple, approximately 1 μm in size, caused by peeling off of eutectic Si particles can be identified. Figures 6(a) and (b) show the whole 3D casting fracture morphology and porosity characteristics of Positions 6 and 5, respectively. Compared with the crack of Position 5, a fracture with a steeper slope and higher porosity exhibits in Position 6, as shown in Figs. 6(a1) and (b1). Figure 6(b) shows a relatively rough fracture surface with a tearing edge and multiple secondary cracks. From Figs. 6(a2) and (b2), it can be found that an instantaneous fracture mode exhibits in Position 6, while a crack growth zone with a relatively rough fracture surface and a 1 mm long platform is present in Position 5. The difference in fracture morphology causes the different mechanical behaviors.

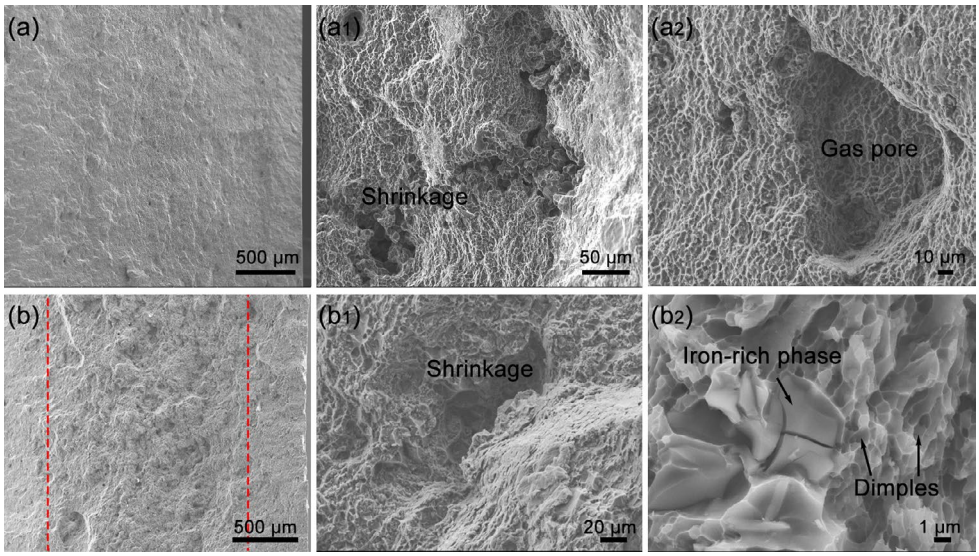

Fig. 5: Whole casting fracture morphology of plate at Position 6 (a), Position 5 (b), and corresponding local fracture characteristics of Position 6 (a1), (a2) and Position 5 (b1), (b2), respectively

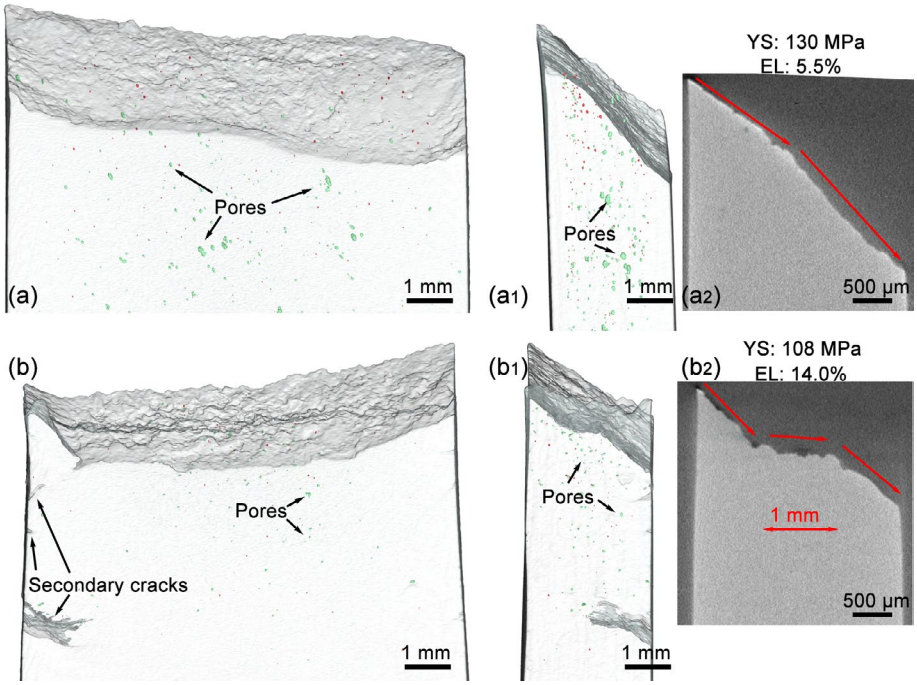

Fig. 6: 3D fracture morphology of Position 6 (a), Position 5 (b) and corresponding 3D side view (a1), (b1), and 2D side view (a2), (b2), respectively

Furthermore, the porosity in Positions 5 and 6 was investigated. As shown in Fig. 7(a), the pores with a larger equivalent diameter always have a lower shape factor and these pores are not single gas pores but a complex combination of gas pore and shrinkage, named gas-shrinkage pores. According to Ref. [19], gas-shrinkage pore is caused by the combined effect of air entrainment and feeding failure in ESC inter-dendritic boundary and it serves as the dominant crack sources promoting the crack propagation. In addition, the lager-scale pores with a relatively higher shape factor are found in Position 6. The presence of higher porosity and larger-sized pores in Position 6 is ascribed to the insufficient filling power. The relatively lower shape factor of pores in Position 5 is closely associated with the insufficient feeding behavior in ESC inter-dendritic boundary and thus the proportion of shrinkage is relatively higher. In Figs. 7(b)–(d), the volume fraction, equivalent diameter, and number of pores in Position 5 are 0.00561%, 35.27 μm, and 264, respectively and all the geometric parameters are lower than those in Position 6 (0.01691%, 40.68 μm, and 352). Position 5 exhibits less than one third of porosity than Position 6, indicating that the shock tower in the near-gate location exhibits a better performance.

To elucidate the disparities in yield strength and elongation, strengthening and plasticity mechanisms are presented, and the microstructural characteristics at near-gate position 5 and far-gate position 6 are listed in Table 4.

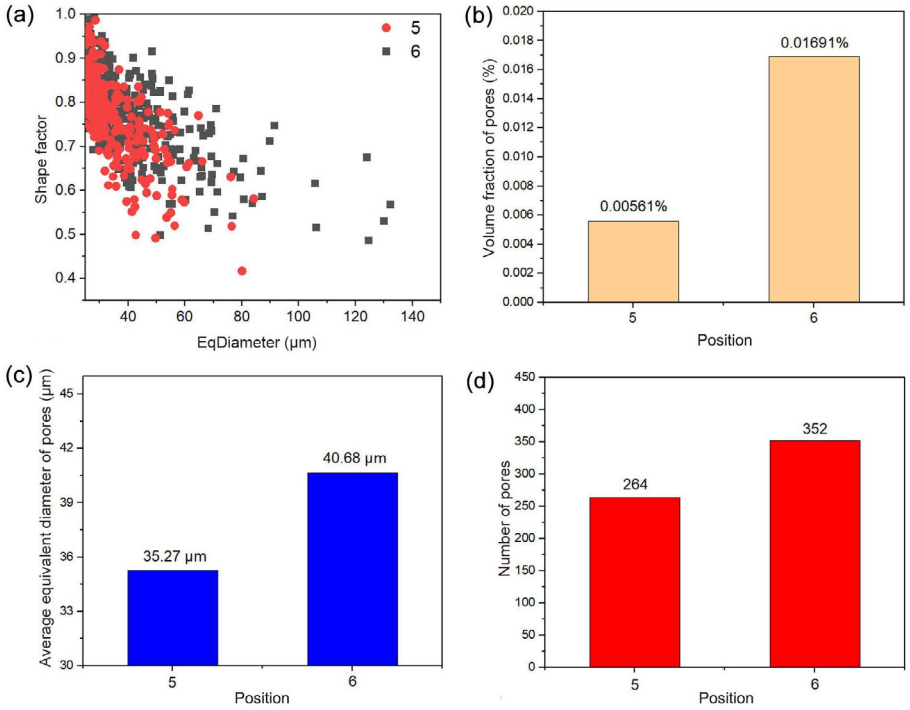

Fig. 7: Shape factor versus equivalent diameter of Positions 5 and 6 (a) and geometric parameters of pores: (b) volume fraction; (c) equivalent diameter; and (d) number

Table 4: Microstructural features at near-gate Position 5 and far-gate Position 6

Sampling position	Grain size (μm)	Si content (wt.%)	Si particles area fraction	Eutectic area fraction	Primary α-Al area fraction	Porosity
5	~20	8.85± 0.18	15.2%	37.7%	62.3%	0.00561%
6	~8	9.80± 0.19	25.3%	40.3%	59.7%	0.01691%

3.4 Yield strength analysis

To verify the validity of the above mentioned analysis and quantitatively assess the contributions of different reinforcements to the mechanical properties of hypoeutectic Al-Si alloys, grain boundary strengthening (σ_g), precipitation strengthening (σ_p), and solid solution strengthening (σ_s) were evaluated. The overall theoretical strength (σ_A) can be formulated as Eq. (1) :

$$\sigma_A=\sigma_g+\sigma_p+\sigma_s \quad (1)$$

where σ_g is calculated by Hall-Petch relation[20]:

$$\sigma_g=\sigma_0+kd^{-\frac{1}{2}} \quad (2)$$

where σ_0 is friction stress, d is average grain size, and k is a constant related to the aluminum (0.12 MPa·$\sqrt{m}$)[21]. The discrepancy in σ_g between Position 5 and Position 6 of plates can be derived using Eq. (3):

$$\sigma_g=k\Delta\left(d^{-\frac{1}{2}}\right) \quad (3)$$

Based on the grain size in Table 4, the $\Delta\sigma_g$ is evaluated to

be 15.6 MPa. The contribution of σ_p is from the Si particles in plastic deformation and it can be expressed by[22, 23]:

$$\sigma_p = \frac{Gb}{2\pi\sqrt{1-\vartheta}\left(\frac{0.779}{\sqrt{f_p}}-0.785\right)d_p}\ln\frac{0.785d_p}{b} \quad (4)$$

where G is shear modulus (27 GPa), b is Burger vector (0.286), ϑ is Poisson ratio of Al matrix (0.33), f_p and d_p are the area fraction and diameter (~1 μm) of Si particles, respectively. From Figs. 4(f) and (g), the spacing of Si particles is similar while the Si particles area fraction in the two different positions is different (15.2% in Position 5 and 25.3% in Position 6). The strengthening effect from dislocation-particle interactions is calculated to be 8.6 MPa in Position 5 and 13.4 MPa in Position 6, and thus $\Delta\sigma_p$ is calculated to be 4.8 MPa. From Ref. [24], yield strength indicates a relatively insensitive dependence on the variation of porosity and the contribution of Si particles can be expressed as follows:

$$YS=18.52+32.88\exp(x/49.31) \quad (5)$$

where x is Al-Si eutectic area fraction and $\Delta\sigma_p$ induced by the disparity in Si particles amounts to 3.8 MPa, which aligns closely with the previously calculated value of 4.8 MPa.

As for σ_s, the solid-solution strengthening effect arises from multiple solutes (such as Si, Fe, V, Zr, and Mn), which can be formulated as follows[25]:

$$\sigma_s = \sum_i^n k_i C_i^{2/3} \quad (6)$$

where k_i is the scale coefficient of element i, C_i is the mass fraction of element i in Al matrix, and n is total element types. The mass fraction of Si atoms in Position 6 is higher than that in Position 5 because of solute enrichment in far-gate region. But it is a complex factor because the contribution of different elements is hard to measured. An indirect method was employed by subtracting grain boundary and precipitation strengthening contributions from measured yield strength. According to Eq. (1), $\Delta\sigma_s$ is calculated as 1.6 MPa, and the strength differences (D-value) between Positions 5 and 6 in the shock tower are listed in Table 5. Grain boundary strengthening, which accounts for nearly 71% ($\Delta\sigma_g/\Delta\sigma_A$) of the strength difference, emerges as the primary contributor to the observed strength variations.

Table 5: Differences in strength (D-value) of Positions 5 and 6 in shock tower

Strength	$\Delta\sigma_g$	$\Delta\sigma_p$	$\Delta\sigma_s$	$\Delta\sigma_A$
D-value (MPa)	15.6	4.8	1.6	22

3.5 Elongation analysis

Compared with Fig. 6(a2), an additional ~1 mm crack propagation platform with a rough serrated shape exhibits in Fig. 6(b2) and it proves the plastic fracture mode. For tensile elongation, it is closely related to porosity and area fraction of Si particles. Lee[26, 27] proposed a total effective void area fraction inside a specified material and it includes two parts: the area fraction of micro-voids, $f_{\text{micro-void}}$, and the additional discontinuous area fraction formed by fracture damage of Si particles, $f_{\text{Si-particles}}$, i.e.:

$$f_{\text{effective void area}} = f_{\text{micro-void}} + f_{\text{Si-particles}} \quad (7)$$

The tensile elongation can be expressed by the following Eq. (8):

$$\varepsilon = \varepsilon_0[1-f_{\text{effective void area}}]^a \quad (8)$$

where ε_0 is the maximum value of achievable in defect-free conditions. a is the defect susceptibility of tensile elongation to microporosity variation. Actually, the the area fraction of Si (15.2% in Position 5 and 25.3% in Position 6) has a direct bearing on the development of ductile dimples and micropores on the fracture surface. According to Ref. [24], the values of a at Positions 5 and 6 are estimated to be approximately 2.7 and 3.0, respectively, and the corresponding ε values are calculated as $0.61\varepsilon_0$ and $0.42\varepsilon_0$, resulting in a difference of $0.19\varepsilon_0$. In addition, from Table 4, larger porosity in Position 6 plate is detected but no precise result to determine the pores on the fracture surface. Actually, the pores near the fracture play a decisive effect on the fracture. Large-sized pores lead to greater stress concentration and facilitate crack propagation, exhibiting a power-law relationship with tensile ductility on the fracture surface[28]. As shown in Figs. 6(a1) and (b1), the plate at Position 6 has more large pores near the fracture, which may be a key factor for its lower elongation. This results in an ε-value difference between Positions 5 and 6 exceeding 0.19. In summary, with over three-fold higher porosity, 66.4% greater $f_{\text{Si-particles}}$, and a larger a value than Position 5, the plate at Position 6 has a significantly lower tensile elongation.

4 Conclusions

(1) In tensile testing of specimens extracted from different locations on the shock tower, the plate from the near-gate position (Position 5), characterized by a microstructure with coarse equiaxed/columnar (ESC) dendrites and lower porosity, exhibits a lower yield strength. In contrast, the plate from the far-gate position (Position 6), which features a finer primary α-Al grain structure but higher porosity, shows significantly reduced elongation, indicating inferior ductility.

(2) Based on the 3D casting fracture morphology and porosity characteristics, the fracture section of the plate at Position 6 exhibits a steeper slope, whereas the fracture interface at Position 5 features a rough crack propagation platform. This contributes to its higher elongation.

(3) The primary strengthening mechanism responsible for the yield strength difference between the near-gate (Position 5) and far-gate (Position 6) regions is grain boundary strengthening, which accounts for approximately 71% of the total contribution. In addition, higher Si area fraction and porosity severely decreases the elongation in far gate (Position 6) region.

Acknowledgments

The authors would like to thank the National Natural Science Foundation of China (Grant Nos. 52405342 and 52175335), the National Key Research and Development Program of China (Grant No. 2022YFB3404201), the Fundamental Research Funds for the Central Universities (Grant Nos. N2302014 and N25ZJL003) and the Natural Science Foundation Joint Foundation of Liaoning province (Grant No. 2023-BSBA-108). The authors also appreciate the help provided by China FAW Foundry Co., Ltd.

Conflict of interest

Prof. Shou-mei Xiong is an EBM of *CHINA FOUNDRY*. He was not involved in the peer-review or handling of the manuscript. The authors have no other competing interests to disclose.

References

[1] Choi H, Koç M, Ni J. Determination of optimal loading profiles in warm hydroforming of lightweight materials. Journal of Materials Processing Technology, 2007, 190: 230–242. https://doi.org/10.1016/j.jmatprotec.2007.02.040.
[2] Raabe D, Ponge D, Uggowitzer P J, et al. Making sustainable aluminum by recycling scrap: The science of “dirty” alloys. Progress in Materials Science, 2022, 128: 100947. https://doi.org/10.1016/j.pmatsci.2022.100947.
[3] Miao B R, Luo Y X, Peng Q M, et al. Multidisciplinary design optimization of lightweight carbody for fatigue assessment. Materials & Design, 2020, 194: 108910. https://doi.org/10.1016/j.matdes.2020.108910.
[4] Miller W S, Zhuang L, Bottema J, et al. Recent development in aluminium alloys for the automotive industry. Materials Science and Engineering: A, 2000, 280: 37–49. https://doi.org/10.1016/S0921-5093(99)00653-X.
[5] Krall P, Weißensteiner I, Pogatscher S. Recycling aluminum alloys for the automotive industry: Breaking the source-sink paradigm. Resources Conservation and Recycling, 2024, 202: 107370. https://doi.org/10.1016/j.resconrec.2023.107370.
[6] Li Y, Li H, Katgerman L, et al. Recent advances in hot tearing during casting of aluminium alloys. Progress in Materials Science, 2021, 117: 100741. https://doi.org/10.1016/j.pmatsci.2020.100741.
[7] Sjölander E, Seifeddine S. The heat treatment of Al-Si-Cu-Mg casting alloys. Journal of Materials Processing Technology, 2010, 210: 1249–1259. https://doi.org/10.1016/j.jmatprotec.2010.03.020.
[8] Chakrabarti D J, Laughlin D E. Phase relations and precipitation in Al-Mg-Si alloys with Cu additions. Progress Material Science, 2004, 49: 389–410. https://doi.org/10.1016/S0079-6425(03)00031-8.
[9] Huttunen-Saarivirta E. Microstructure, fabrication and properties of quasicrystalline Al-Cu-Fe alloys: A review. Journal of Alloys and Compounds, 2004, 363: 154–178. https://doi.org/10.1016/S0925-8388(03)00445-6.
[10] Bendo A, Matsuda K, Lee S, et al. Microstructure evolution in a hydrogen charged and aged Al-Zn-Mg alloy. Materialia, 2018, 3: 50–56. https://doi.org/10.1016/j.mtla.2018.09.035.
[11] Liu F, Zheng H, Zhong Y, et al. Effect of Cu/Mg-containing intermetallics on the mechanical properties of the as-cast HVDC AlSiMgMnCu alloys by SBFSEM at nano-scale. Journal of Alloys and Compounds, 2022: 166837. https://doi.org/10.1016/j.jallcom.2022.166837.
[12] Jiao X, Liu C, Wang J, et al. On the characterization of microstructure and fracture in a high-pressure die-casting Al-10wt.%Si alloy. Progress in Natural Science: Materials International, 2020, 30: 221–228. https://doi.org/10.1016/j.pnsc.2019.04.008.
[13] Basavakumar K G, Mukunda P G, Chakraborty M. Influence of grain refinement and modification on microstructure and mechanical properties of Al-7Si and Al-7Si-2.5Cu cast alloys. Materials Characterization, 2008, 59: 283–289. https://doi.org/10.1016/j.matchar.2007.01.011.
[14] Timpel M, Wanderka N, Schlesiger R, et al. The role of strontium in modifying aluminium-silicon alloys. Acta Materialia, 2012, 60: 3920–3928. https://doi.org/10.1016/j.actamat.2012.03.031.
[15] Zamani M, Morini L, Ceschini L, et al. The role of transition metal additions on the ambient and elevated temperature properties of Al-Si alloys. Materials Science and Engineering: A, 2017, 693: 42–50. https://doi.org/10.1016/j.msea.2017.03.084.
[16] Luo A A, Sachdev A K, Apelian D. Alloy development and process innovations for light metals casting. Journal of Materials Processing Technology, 2022, 306: 117606. https://doi.org/10.1016/j.jmatprotec.2022.117606.
[17] Zhang Y, Lordan E, Dou K, et al. Influence of porosity characteristics on the variability in mechanical properties of high pressure die casting (HPDC) AlSi7MgMn alloys. Journal of Manufacturing Processes, 2020, 56: 500–509. https://doi.org/10.1016/j.jmapro.2020.04.071.
[18] Zheng H, Jiang Y, Liu F, et al. Microstructure heterogeneity optimization of HPDC Al-Si-Mg-Cu alloys by modifying the characteristic of externally solidified crystals. Journal of Alloys and Compounds, 2024, 976: 173167. https://doi.org/10.1016/j.jallcom.2023.173167.
[19] Li X, Xiong S M, Guo Z. Correlation between porosity and fracture mechanism in high pressure die casting of AM60B alloy. Journal of Materials Science & Technology, 2016, 32: 54–61. https://doi.org/10.1016/j.jmst.2015.10.002.
[20] Meyers M A, Mishra A, Benson D J. Mechanical properties of nanocrystalline materials. Progress Material Science, 2006, 51: 427–556. https://doi.org/10.1016/j.pmatsci.2005.08.003.
[21] Nie J F. Effects of precipitate shape and orientation on dispersion strengthening in magnesium alloys. Scripta Materialia, 2003, 48: 1009–1015.
[22] Wang Y, Zhao Y, Xu X, et al. Superior mechanical properties induced by the interaction between dislocations and precipitates in the electro-pulsing treated Al-Mg-Si alloys. Materials Science and Engineering: A, 2018, 735: 154–161.
[23] Wang C, Dong Z, Jiang B, et al. Lowering thermal expansion of Mg with the enhanced strength by Ca alloying. Journal of Materials Research and Technology, 2023, 24: 1293–1303.
[24] Lee C, Youn J, Lee Y, et al. Effect of eutectic Si particles on the defect susceptibility of tensile properties to microporosity variation in Al-*x*Si binary alloys. Materials Science and Engineering: A, 2016, 678: 227–234.
[25] Esmaeili S, Lloyd D J, Poole W J. A yield strength model for the Al-Mg-Si-Cu alloy AA6111. Acta Materialia, 2003, 51: 2243–2257. https://doi.org/10.1016/S1359-6454(03)00028-4.
[26] Lee C D. Variability in the tensile properties of squeeze-cast Al-Si-Cu-Mg alloy. Materials Science and Engineering: A, 2008, 488: 296–302. https://doi.org/10.1016/j.msea.2007.11.014.
[27] Lee C D. Effect of damage evolution of Si particles on the variability of the tensile ductility of squeeze-cast Al-10%Si-2%Cu-0.4%Mg alloy. Materials Science and Engineering: A, 2010, 527: 3144–3150. https://doi.org/10.1016/j.msea.2010.01.061.
[28] Lordan E, Zhang Y, Dou K, et al. On the probabilistic nature of high-pressure die casting. Materials Science and Engineering: A, 2021, 817: 141391. https://doi.org/10.1016/j.msea.2021.141391.